GEOPHYSICS, VOL. 85, NO. 5 (SEPTEMBER-OCTOBER 2020); P. EN63–EN76, 11 FIGS., 2 TABLES.
10.1190/GEO2019-0539.1

Estimation of the top of the saturated zone from airborne electromagnetic data

Noah Dewar[1] and Rosemary Knight[1]

ABSTRACT

In an airborne electromagnetic (AEM) data set acquired in unsaturated and saturated zones, the depth of the top of the saturated zone (TSZ) at the time of data acquisition should be accounted for in the resistivity-to-lithology transform. We have developed and tested a methodology for estimating the TSZ from AEM data, using data collected in three survey areas in the Central Valley of California and water-table elevation (WTE) measurements from nearby wells. The methodology is based on the difference in the distribution of resistivity values above and below the TSZ, using the WTE measurements to optimize two components of the general workflow. From the AEM data acquired in Tulare County, in the southern portion of the Central Valley, where the WTE measurements were acquired two to four weeks before the AEM data acquisition, we have found estimates of the TSZ with a root-mean-square (rms) error of 10.6 m when compared to the WTE measurements. From the two survey areas in Butte and Glenn counties, in the northern portion of the Central Valley, where WTE measurements were available at the time of, and closer to the locations of, AEM data acquisition, we have found estimates of the TSZ with an rms error ranging from 3.8 to 5.3 m, depending on the form of inversion. The level of error found in the three survey areas is comparable to the thickness of the layers in the resistivity models at the depths of the TSZ. Because the intended use of these estimates is to locate the TSZ for use in developing and applying the resistivity-to-lithology transform, the level of error associated with this new methodology is acceptable.

INTRODUCTION

Concern about the sustainability of groundwater resources has led to a growing recognition of the need for more effective management. A major challenge typically encountered in groundwater management is the limited information available about the spatial extent and connectivity of aquifers and aquitards, making it difficult to accurately predict the response of the groundwater system to changes in climate, land use, groundwater pumping, and other activities (Faunt, 2009; Binley et al., 2015).

The airborne electromagnetic (AEM) method is a geophysical technique that can provide the data required to develop a model of the large-scale architecture of groundwater systems (Cook and Kilty, 1992; Fitterman and Deszcz-Pan, 2001; Paine, 2003; Chongo et al., 2015; Høyer et al., 2015; Podgorski et al., 2015; Foley et al., 2016; Knight et al., 2018). After processing and inverting the acquired AEM data, a model of subsurface electrical resistivity is obtained. One approach to using a derived resistivity model to map the architecture of the groundwater system is to transform the resistivity model into a lithology model. The required transform, known as a rock physics or resistivity-to-lithology transform, can be developed using colocated AEM and lithology data, such as those obtained from drillers' logs (Christiansen et al., 2014; Foged et al., 2014; Knight et al., 2018). The accuracy of the resistivity-to-lithology transform directly affects the accuracy of the derived representation of the groundwater system.

The AEM study by Knight et al. (2018) in the Central Valley of California highlights the importance of accounting for the saturation state when transforming resistivity to lithology. Given the impact of water content on resistivity, we expect the range of resistivity values corresponding to the various lithologic units at a site to change at the top of the saturated zone (TSZ), the depth at which the saturation

Manuscript received by the Editor 6 August 2019; revised manuscript received 28 April 2020; published ahead of production 11 June 2020; published online 14 July 2020.
[1]Stanford University, Department of Geophysics, Stanford, California 94305-2215, USA. E-mail: ndewar@stanford.edu (corresponding author); rknight@stanford.edu.

DOI:10.1190/geo2019-0539.1

state transitions from unsaturated (containing water and air) to fully water-saturated. To account for the effects of saturation state on resistivity in developing and applying a resistivity-to-lithology transform, the depth to the TSZ must be known at all AEM measurement locations at the time of AEM data acquisition. This will be most important in areas where a significant portion of the AEM data are from the unsaturated zone, as was the case in the study in the Central Valley.

Knight et al.'s (2018) study assumed that the water table elevation (WTE) was equivalent to the TSZ. Thus, to account for and reveal the impact of saturation on resistivity, an interpolated map of WTE provided by the California Department of Water Resources (DWR) was used. We note that the assumption that the TSZ is the same as the WTE is not always correct. If there is a capillary fringe (a layer of fully saturated sediments above the water table in which water is held in the pore space due to capillary forces), the TSZ will be at the top of the capillary fringe. In the vertically layered fluvial depositional environment of the Central Valley of California, however, the thickness of the capillary fringe is limited by the presence of thin layers of coarse sediments. This suggests that even in locations where there is a capillary fringe, it will be sufficiently thin, given the resolution of the AEM data, so as to have a negligible impact on the acquired data; thus, it is reasonable in this area to assume that the WTE is equivalent to the TSZ.

However, there are two general limitations to the approach taken by Knight et al. (2018) regardless of the survey area. The first limitation is the low spatial resolution of the WTE measurements available from the DWR. The WTE maps from the DWR typically have a spatial resolution on the order of kilometers, so they are unlikely sufficient to capture the spatial variability in the depth to the TSZ throughout the region covered by a typical AEM survey. The second and most critical limitation is the timing of the measurements. The DWR measurements typically are made twice a year, so they are unlikely to provide information at the time of the AEM survey due to seasonal variation. Therefore, although the approach taken by Knight et al. (2018) proved useful for the purposes of that study, it should not be adopted as a standard methodology for accounting for the impact of the saturation state on AEM resistivity measurements. We are thus motivated to find a way to estimate the TSZ from the AEM data. This would allow us to map the temporally varying TSZ, at the time of AEM acquisition, at all locations where AEM data are acquired, providing the information needed about saturation state to develop and apply an accurate resistivity-lithology transform.

Estimation of TSZ from AEM data acquired in a geologically heterogeneous environment is challenging because spatial variation in lithology, and the corresponding variation in resistivity, can mask the change in resistivity associated with a change in water content. It is thus highly unlikely that the TSZ could be identified in the AEM data by examining a 1D model of resistivity as a function of depth at a single location. However, we expect that sediments in the saturated zone will have values of electrical resistivity that belong to a distribution different from that containing resistivity values for sediments in the unsaturated zone. In the Knight et al. (2018) study, the distribution of resistivity values changed in two ways in going from the unsaturated zone to the saturated zone. The distribution shifted to lower values because all materials will be less resistive when saturated, and the distribution narrowed given the reduced range in saturation. A promising approach is to use the change in the resistivity distribution across the TSZ to identify the depth of the TSZ. In areas with variable water quality, the salinity of the water is another factor that will influence subsurface resistivity and must be accounted for. Reports describing water quality in the survey areas indicate that this was not an issue in any of the three areas investigated in this study (Luhdorff and Scalmanini Consulting Engineers, 2016; Peterson, 2018).

A recent study (Behroozmand et al., 2019) involving the use of a ground-based electromagnetic (EM) system tackled the same problem — that is, the need to locate the TSZ to determine a resistivity-lithology transform. The assumption made was that there would be a change in the resistivity distribution at the TSZ. For each agricultural field (approximately 0.2 km^2) in which EM data were acquired, distributions of resistivity values over the entire field were created for regularly spaced depth intervals. These vertical stacks with a different resistivity distribution at each depth interval, referred to in this paper as depth-registered resistivity distributions, were manually examined to estimate the depth to the TSZ. This method, while promising, relied on manual interpretation of the inverted resistivity data, so it is subjective and would be very time-consuming if applied at the scale of an AEM survey. We built on the concepts presented in the Behroozmand et al. (2019) study (direct estimation of the TSZ from the distributions seen in the inverted resistivity data) to design a methodology appropriate for a typical AEM survey.

Our goal in this study was to develop a methodology that, at the time of the AEM survey, allows us to obtain an estimate of the depth to the TSZ at all locations where AEM data are available. The methodology was designed to use measurements of WTE from wells to optimize the workflow parameters that are likely to be site-specific and thus vary between AEM survey areas. We applied our methodology to three different AEM data sets: two acquired in December 2018 and another acquired in October 2015. The use of this methodology leverages the collected AEM data to obtain information about the saturation state; this is critical for interpreting resistivity data. The ability to account for the saturation state in developing and applying a resistivity-lithology transform is essential for the reliable interpretation of AEM data in areas where the water table is sufficiently deep such that a significant portion of the data are acquired in the unsaturated zone.

The three AEM data sets used in the development and testing of the methodology presented in this study were collected in the Central Valley of California using the SkyTEM method. This helicopter-deployed, time-domain AEM method was developed in Denmark for hydrogeologic and environmental mapping (Sørensen and Auken, 2004). Different SkyTEM systems have been developed to specifically target shallow or deeper structures in the subsurface; in this study, we used three different systems. The following background sections provide additional information about the survey areas in the Central Valley of California where AEM data were acquired and on the specific time-domain AEM method used in this study.

BACKGROUND

Survey areas in Butte and Glenn counties

In 2018, AEM data were acquired in Butte and Glenn counties in the northern section of the Central Valley, known as the Sacramento Valley. Figure 1 shows the survey areas and, on the inset map, their locations within California. The AEM data were acquired in two distinct areas with two different AEM systems. The SkyTEM

DOI:10.1190/geo2019-0539.1

method uses a dual high/low moment setup in which the system switches back and forth between two different current waveforms during data acquisition. The high moment provides information about deeper structures, whereas the low moment resolves finer structures in the near surface. The SkyTEM 312 system was used in the western survey area, referred to as the 312 survey area, which covers parts of Butte and Glenn counties, whereas the SkyTEM 304 system was used in the eastern survey area, referred to as the 304 survey area, which is entirely in Butte County. The main difference between the two areas, besides the system used, is that the 304 survey area includes the start of the foothills at the edge of the valley and thus contains a greater variation in elevation.

The sediment character of the Sacramento Valley differs from the rest of the Central Valley due to the presence of deposits of volcanic tuff interlayered with fluvial sediments sourced from volcanic features, such as the Sutter Buttes (Bryan, 1923). In the Butte County portion of the survey areas, some of the flight lines extend into the foothills at the edge of the Central Valley. Whereas the shallow subsurface mostly consists of coarse-grained sediments with fine-grained lenses, we expect the deeper subsurface structure to be heterogeneous and contain multiple layers of varying resistivity dipping up from the center of the valley toward the foothills at the valley wall (Greene and Hoover, 2014).

Tulare County survey area

The 2015 AEM data set was acquired with the SkyTEM 508 system in Tulare County in the southern portion of the Central Valley, the San Joaquin Valley. The location of the survey area in California is shown in Figure 2 on the inset map. In the San Joaquin Valley, the upper and lower aquifer units are made up of a mix of alluvium from the Coast Ranges and the Sierra Nevada along with many small lenses of clay (Faunt, 2009). Throughout much of the survey area the two aquifers are separated by a clay layer, varying in thickness from 0 to 20 m, at an approximate depth of 100 m; this clay layer is referred to as the Corcoran Clay (Faunt, 2009).

Time-domain AEM method

Time-domain AEM systems function by using a transmitter coil to induce electrical currents in the ground as described by Faraday's law of induction. When the transmitter is shut off, the decay of the induced eddy currents induces a response in a receiver coil. This measured response is referred to as a transient, and it contains information about the resistivity structure of the subsurface. After removing transients contaminated with noise originating from infrastructure such as power lines, the data are processed using trapezoidal and moving average filters (the trapezoidal filter has a width of 4 s near the surface and 18 s at depth), and they are then stacked to improve the signal-to-noise ratio (S/N) (Sørensen and Auken, 2004). For the systems used in this study, tens to hundreds of transients are stacked to produce a single data point, resulting in approximately 30 m separating adjacent data points, depending on the flight speed (Sørensen and Auken, 2004). This stacking and horizontal filtering will have the effect of averaging any measured response along the flight direction. This is not an issue for the purpose of this study because the length scale over which this averaging occurs is below the length scale over which the TSZ varies. After the AEM data set has been through quality control and processing (see Asch et al., 2019 for details) it is ready for inversion.

The AEM data used in this study were inverted for subsurface resistivity using the spatially constrained 1D inversion module in the Aarhus Workbench (Auken et al., 2009; HydroGeophysics Group, 2011; Auken et al., 2015). In the Tulare survey area, a semi-sharp inversion was produced using a uniform starting model of 30 ohm-m. In each of the 312 and 304 survey areas, we produced one smooth and one sharp inversion, all with a uniform starting model of 10 ohm-m. In the Aarhus Workbench, the smooth and sharp inversions differ in that the sharp inversion algorithm penalizes the number of resistivity changes, not the magnitude of the resistivity changes, as is done by the smooth inversion algorithm (Vignoli et al., 2015). These different inversions were produced to assess the effect of varying the type of inversion on the developed methodology for locating the TSZ.

The footprint of the AEM measurement is dependent on the flight height and background geology and is on average approximately

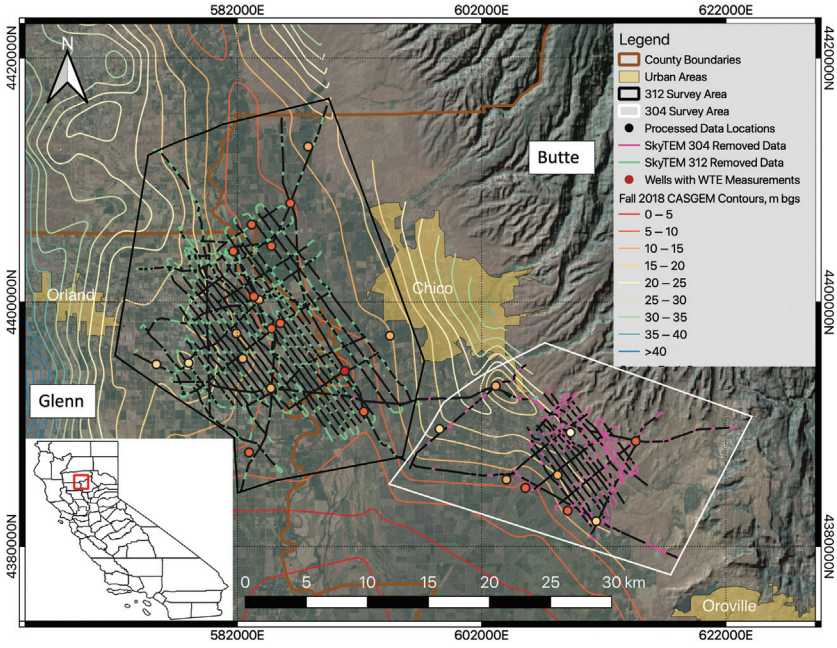

Figure 1. The red square on the inset map shows the location of the survey areas in the state of California. The black lines on the inset map are county boundaries. The dark-brown lines on the main map mark county boundaries with Glenn County in the west and Butte County in the east. The light-brown shading indicates urban areas. The black and white polygons indicate the 312 and 304 survey areas, respectively. The locations of the final processed data are marked by the black dots. The light-green and pink lines, respectively, show the portions of the 312 and 304 flight lines where data were removed. The contour lines show the depth to the water table from the fall 2018 CASGEM measurements retrieved from https://gis.water.ca.gov/app/gicima/ (California Department of Water Resources, 2020a). The colored circles indicate the locations of the wells with WTE measurements, with the color-coding matching that of the contours. The base imagery is sourced from Google, Landsat/Copernicus.

60 m at the surface and it increases with depth (Madsen et al., 2017). The tilt of the AEM transmitter also influences the footprint. Due to the rigid geometry of the SkyTEM transmitter, during normal flight conditions, the average tilt is less than 10 degrees. The impact on the acquired data of this low-angle tilt can be corrected during standard data processing (Auken et al., 2009). The footprint provides a rough estimate of the horizontal resolution that can be obtained with the AEM method.

The vertical resolution of the AEM method depends on the system used, the flight height, and the resistivity structure in the subsurface; therefore, it can vary throughout an AEM survey area. Generally, the thickness of the layers in the final resistivity model is taken as an indication of the vertical resolution of the AEM method. The thickness of the layers depends on numerous parameters such as the inversion setup, the spatial constraints applied during the inversion, and the filtering and processing applied to the data, but it typically will range from values on the order of meters close to the surface to tens of meters at depth. We note that although assuming an equivalence between layer thickness and resolution is reasonable for the inversion methods used in this study, this will not be the case when using methods that solve for the layer thickness. In this study, we did not investigate the efficacy of our developed methodology when applied to resistivity models acquired through the use of these other types of inversions.

To determine at what depth the resistivity values in the final model no longer are reliable, we apply a concept known as the depth of investigation (DOI) (Spies, 1989). In this study, where our objective was to map out the water table in the shallow subsurface, the DOI had no impact on our results.

DESCRIPTION OF DATA

AEM and water table data in Butte and Glenn counties

The AEM data in Butte and Glenn counties were acquired between 30 November and 4 December 2018, with the 312 and 304 SkyTEM systems over the two survey areas. The 312 survey area covered approximately 600 km^2 and contained 585 line kilometers, whereas the 304 survey area covered approximately 500 km^2 and contained 224 line kilometers. The average flight speed and flight height were 94 km/h (26 m/s) and 42 m, respectively, for the 312 survey area, and 90 km/h (25 m/s) and 38 m, respectively, for the 304 survey area. Technical details for the SkyTEM systems can be found in Appendix A. The 312 system was designed for improved depth of reliable imaging, to better characterize deep structures, whereas the 304 system was designed for resolving fine near-surface structures. For dual-moment AEM systems, improving the near-surface resolution will reduce the depth of reliable imaging, and vice versa. Thus, the 304 has a shallower total depth of imaging whereas the 312 has reduced near-surface resolution. The vertical thickness of the layers in the resistivity models produced from the 312 data varies from 3.0 m at the surface to 38.5 m at a depth of 550 m; in the 304 data, it varies from 1.0 m at the surface to 34.2 m at a depth of 375 m.

In the 312 survey area, the important hydrostratigraphic units are located farther below the surface due to the dipping structure and distance from the valley's edge. The 312 system, with its increased resolution at depth, was used to acquire the AEM data in this area. In the 304 survey area, the objective was high-resolution mapping of near-surface recharge pathways. Due to the different system parameters and the distance separating the 312 and 304 survey areas, the two data sets were processed, inverted, and analyzed separately in this study. The flight lines along which the data in the 312 and 304 survey areas were collected are shown in Figure 1. The spacing of the flight lines varied due to infrastructure and other flight obstacles, but it was approximately 500 m for the closely spaced grid lines and approximately 2 km for the perpendicular control lines. Given our interest in the development of a methodology for locating the TSZ that would involve the use of well measurements of the WTE, we located the flight lines as close as possible to the wells from which we planned to obtain WTE measurements.

A challenge that we encountered during data acquisition in the 304 survey area was the high density of powerlines including one large high-voltage transmission line. As seen in Figure 1, this resulted in the removal of data in a relatively large number of areas as compared to the 312 survey area.

We calculated an average groundwater gradient of 0.6 m/km in the 312 area and 1.1 m/km in the 304 area from the WTE data available over the two survey areas. Given that our approach involves using the well-based measurements of WTE as estimates of the depth to the TSZ in the AEM data, we wanted changes in the WTE between the locations of the WTE measurements and the acquired AEM data to be smaller than the vertical layer thickness in the resistivity models at the AEM data locations. We selected a conservative limit of approximately 1 m change in WTE, which is approximately a factor of two less than the vertical layer thickness of the resistivity models (3.7 m in the 312 area, 2.1 m in the 304 area) at the average depth below the ground surface of the WTE. This resulted in the selection of wells for testing and validation that were no greater than 2 km away from the AEM data in the 312 area and 1 km away in the 304 area. Where information about the screened interval of the wells was available, we used this information to remove wells screened in deeper aquifers because the WTE measured in these wells may be different from wells screened in shallow aquifers. These two filtering measures taken together provided 19 wells in the 312 area and 10 wells in the 304 area.

Of the 29 wells available for testing and validation, 22 of them (16 in the 312 area and 6 in the 304 area) are continuously monitored wells built and maintained by the DWR. The data for these wells were downloaded from the state-run Water Data Library (California Department of Water Resources, 2020b). The WTE measurements between 30 November and 4 December (the time period of the AEM data acquisition) were averaged to produce a single measurement of WTE for each well. The difference between the maximum and minimum WTE over this five-day period was approximately 0.2 m, significantly less than the minimum layer thickness in the resistivity models in the 312 and 304 areas at the average WTE.

The remaining seven wells used for testing and validation (three in the 312 area and four in the 304 area) are part of the DWR's California Statewide Groundwater Elevation Monitoring (CASGEM) program; the WTE measurements were downloaded from the Groundwater Information Center Interactive Map Application (GICIMA) website (California Department of Water Resources, 2020a). Additional WTE measurements were made in the selected CASGEM wells, by colleagues at the DWR in the Glenn County wells and the Butte County Department of Water and Resource Conservation in the Butte County wells, the week that the AEM data were collected.

The locations of all of the wells used in the 312 and 304 areas are shown in Figure 1. The distance between the wells and the closest AEM 1D resistivity models ranged from 7 to 1691 m in the 312 area and 85 to 851 m in the 304 area. The final set of combined WTE measurements, from the continuously monitored wells and the CASGEM wells, varied from 32 to 42 m and 27 to 66 m relative to mean sea level (MSL) in the 312 and 304 areas, respectively (7–17 m below ground surface (bgs) in the 312 area and 6–23 m bgs in the 304 area).

AEM and water table data in Tulare County

The AEM data in the Tulare County survey area, presented in Knight et al. (2018), were collected with the 508 SkyTEM system on 27 October 2015. In the Tulare County survey area, 104 total line kilometers were collected with an average flight speed and height of 90 km/h (25 m/s) and 37 m, respectively. A description of the technical specifications of this system can be found in Appendix A. The 508 was selected as the best system available, at the time of the survey, for imaging the deeper structures of the groundwater system. We used the 1D resistivity models along the acquisition flight lines. Figure 2 shows the locations of the flight lines. The flight line spacing was approximately 1 km, and the final 1D resistivity models were separated on average by 35 m along the flight lines. The data had been processed and inverted in the Aarhus Workbench using a 30 layer, semismooth, spatially constrained inversion (Auken et al., 2009; HydroGeophysics Group, 2011). This AEM data set covers an area of approximately 100 km^2 in the Tulare Irrigation District (TID) in Tulare County. The vertical thickness of the layers in the final resistivity models varied from 3 m at the surface to 60 m at a depth of 500 m.

In the Tulare survey area, the regional groundwater gradient was calculated to be 1.1 m/km. We selected WTE measurements to use that were no greater than 2 km from the AEM data. This separation distance corresponded to an estimated variation of approximately 2 m in the WTE, less than the 8.5 m layer thickness in the full resistivity model at the average depth below the ground surface of the WTE in this area; this resulted in 26 available wells for the testing and validation of the developed methodology. As discussed in the previous section, when the information was available, the screened interval depth was used to remove wells with deep screens.

In total, 14 of the WTE measurements were collected as part of the CASGEM program and were downloaded from the GICIMA website (California Department of Water Resources, 2020a); the locations are shown in Figure 2. An additional 12 WTE measurements, made and provided by the TID, also were used, but their locations are confidential and are not shown. The WTE measurements varied from 5 to 45 m relative to MSL (44–61 m bgs) and were collected between 28 September and 14 October 2015. The distance between the WTE measurement locations and the closest 1D resistivity models ranged from 106 to 1822 m.

With two exceptions, the WTE measurements were made in active irrigation wells, so they could have been affected by localized drawdown due to groundwater pumping. Well users are asked to stop pumping 24 hours before any WTE measurements are made (Laird et al., 2016), but the time required to return to equilibrium depends on the local hydrogeology (Fetter, 2000), so this duration may be insufficient. An additional factor that could impact WTE measurements is the effect of nearby wells with continued pumping at the time of measurement.

METHODOLOGY

Our goal was to develop a methodology that could be implemented in any area where AEM data were acquired to locate the TSZ using the 1D resistivity models derived from the AEM data. The key assumption is that there is information in the resistivity data that can be used to locate the TSZ. The specific workflow that is optimal for locating the TSZ will be site-specific, so it must be defined for each survey area. The flowchart in Figure 3 presents our developed methodology for finding the optimal workflow in a survey area, and the following paragraphs describe this procedure. White boxes in the flowchart indicate inputs or results. The letters in round brackets are the variable representation of the quantity in

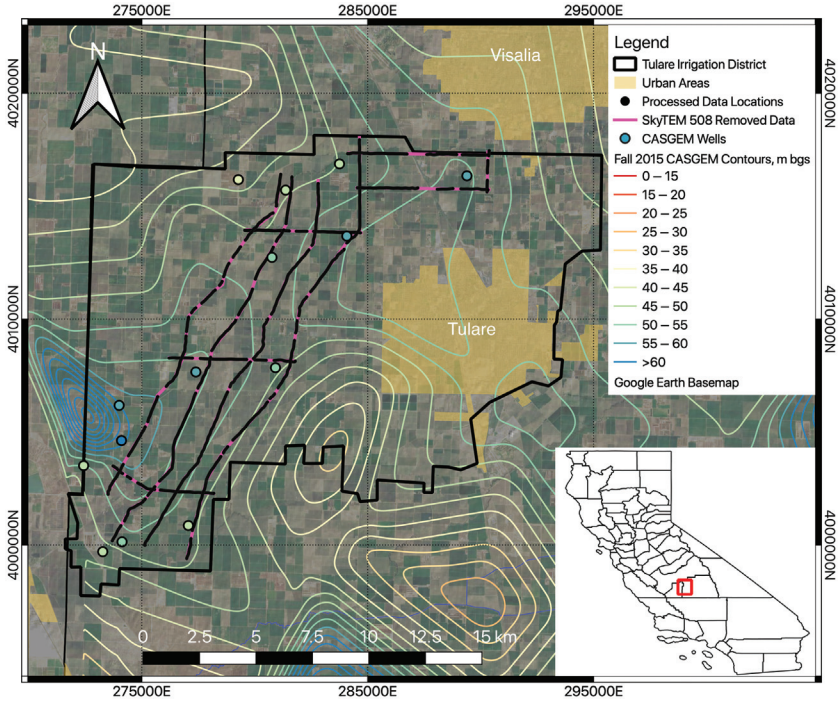

Figure 2. The red square on the inset map shows the location of the Tulare County survey area in the state of California. The black lines on the inset map are county boundaries. The black boundary on the main map represents the boundaries of the Tulare Irrigation District (TID). The light-brown shading indicates urban areas. The locations of the final processed data are indicated with black dots. The pink lines show the portions of the 508 flight lines where data were removed. The contour lines show the depth to the water table from the fall 2015 CASGEM measurements retrieved from https://gis.water.ca.gov/app/gicima/ (California Department of Water Resources, 2020a). The colored circles indicate the locations of the CASGEM wells with WTE measurements with the color-coding matching that of the contours. The base imagery is sourced from Google, Landsat/Copernicus.

DOI:10.1190/geo2019-0539.1

the box. The gray boxes indicate processes or actions. The light-blue boxes indicate loops, where an action or sequence of actions is repeated.

As discussed in our description of the available data in the survey areas, an initial step is identifying the locations of all of the WTE measurements to be used for the testing and validation required to develop and optimize the workflow. In the first action, labeled "select closest 1D resistivity model to each WTE" in Figure 3, we select each of the WTE measurements and find the location of the closest 1D resistivity model, defining this as a location at which we will estimate the TSZ, referred to as a TSZ estimation location (EL). We thus have as many TSZ ELs as we have WTE measurements. The box labeled "estimation locations (EL)" represents the selected TSZ estimation locations. The average distance between the ELs and their corresponding WTE measurements was approximately 200 m for the 312 survey area, approximately 360 m for the 304 survey area, and approximately 600 m for the Tulare survey area.

The next part of our workflow involves repeating a series of actions that involve analysis of the resistivity data, for every EL, and a combination of search radius and statistical property. These are shown in the section of Figure 3 labeled "resistivity data analysis." For a given EL, we set a search radius and gather all of the 1D resistivity models within the search radius from the EL. This circular area defined by the search radius is referred to as the estimation domain. This step is labeled, "gather all 1D resistivity models within SR_j of EL_i," where EL_i is the *i*th estimation location and SR_j is the *j*th search radius. We then define regular depth intervals, over a predefined depth window, and sample the gathered 1D resistivity models to create depth-registered resistivity distributions labeled "construct depth-registered resistivity distributions within predefined depth window." In this study, we used 1 m as the thickness of the regular depth intervals to ensure that they were as small as the thinnest layer in a 1D resistivity model. The predefined depth interval is set to cover the range of possible depths for the TSZ given the recent variation in WTE in the survey area. We used the range of 2–30 m bgs for the 312 and 304 survey areas and 30 to 100 m bgs for the Tulare survey area; these selected depth ranges were based on an analysis of several years of CASGEM WTE data.

The search radius is one of the parameters to be optimized for in a given survey area. The TSZ will introduce changes in the resistivity distribution that occur at one depth. We define this as the "signal" that we seek to recover from our data (the depth-registered resistivity distributions). We recognize that a lithologic variation occurring at a consistent depth, over a lateral distance similar to that over which the depth to the TSZ is constant, could be falsely identified as the TSZ signal. However, we assume that such a lithologic change is unlikely to occur within the predefined depth window for which we search for the TSZ. We, therefore, treat the lithologic variation that can introduce changes in the resistivity distribution as "geologic noise." Because we increase the search radius but stay within a region in which the depth to the TSZ remains constant (i.e., it changes less than the layer thickness of the resistivity model), we increase the S/N. In this study, we used 5 km in all survey areas as the maximum search radius; at this distance, the expected variation in the TSZ, based on the calculated groundwater gradients, will exceed the layer thickness in the resistivity models at the average TSZ depth. Given the along-line spacing of the resistivity models of approximately 30 m, the search radius was increased in increments of 50 m so as to always add at least one more 1D resistivity model to the estimation domain. A maximum of 5 km and increments of 50 m resulted in using every multiple of 50 m from 50 to 5 km as a search radius. In the flowchart, the step showing the input of the search radii to be used is labeled "search radii (SR)."

Starting with the resistivity distribution for each 1 m depth interval, we then want to quantify a change in the character of the distribution that is likely to occur at the TSZ due to the impact of the change in the saturation state on resistivity. The statistical property of the distribution that best captures the transition from the unsaturated to the saturated zone is the second parameter that must be optimized in the workflow. Therefore, we calculate six statistical properties of a distribution that are likely to be affected by the change in saturation state: the minimum, the mean, the maximum, the difference between the 75th and the 25th percentiles, the difference between the maximum and the minimum, and the standard deviation. The step associated with the input of the statistical properties to be tested is labeled

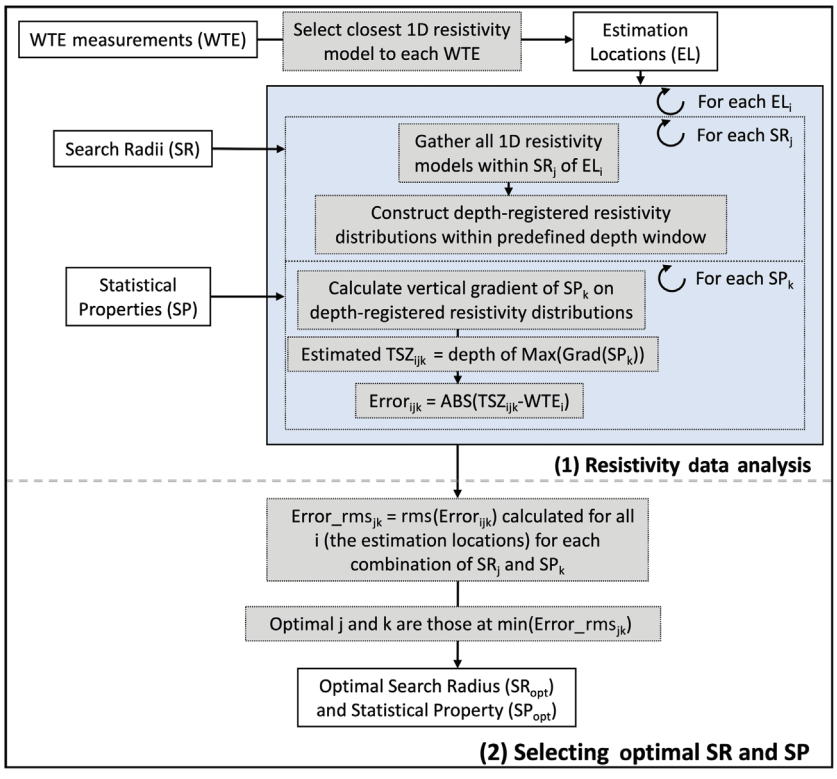

Figure 3. Flowchart illustrating the methodology developed in this study. The bold text in the bottom right describes what is done within each section. The white boxes indicate inputs and results, the gray boxes indicate processes or actions, and the blue boxes indicate loops. The letters in round brackets at the end of a label indicate the variable associated with that box.

DOI:10.1190/geo2019-0539.1

"statistical properties (SP)" in the flowchart. We quantify the change in these properties with depth, that is, the vertical gradient, and we identify the depth at which the maximum in the gradient occurs as the TSZ depth. These steps are labeled "calculate vertical gradient of SP_k on depth-registered resistivity distributions" and "estimated TSZ_{ijk} = depth of max (grad (SP_k))," where SP_k is the *k*th statistical property, and TSZ_{ijk} is the TSZ estimate for the *i*th estimation location, the *j*th search radius, and the *k*th statistical property.

The TSZ estimation process described above is repeated at every EL in a given survey area, for every combination of search radius and statistical property. In the flowchart, the light-blue boxes with circular arrows and the text "for every EL_i," "for every SR_j," and "for every SP_k" show the loops over all of the estimation locations, search radii, and statistical properties, respectively.

We then move into the final stage, labeled "selecting optimal SR and SP." We compare each set of produced TSZ estimates, one for each combination of search radius and statistical property, to the WTE measurements. This comparison is the step labeled "$error_{ijk}$ = ABS (TSZ_{ijk}−WTE_i)" in Figure 3, where TSZ_{ijk} is as described above and $error_{ijk}$ is the absolute difference between TSZ_{ijk} and WTE_i, the *i*th WTE measurement. Next, we calculate the root-mean-square (rms) error for each combination of search radius and statistical property. This step is labeled "$error\_rms_{jk}$ = rms ($error_{ijk}$) for all i (the ELs) for each combination of search radius and statistical property," where $error\_rms_{jk}$ is the rms error associated with the *j*th search radius and the *k*th statistical property. We define the globally optimal combination of search radius and statistical property for an AEM survey area as that which yields the minimum rms error between the TSZ estimates and the WTE measurements. This step is labeled "optimal j and k are those at min ($error\_rms_{jk}$)," whereas the step indicating the selection of the globally optimal combination is labeled "optimal search radius (SR_{opt}) and statistical property (SP_{opt})."

Figure 4 shows an example of the resistivity data analysis for one of the ELs in the 312 survey area. Shown schematically in Figure 4a is the gathering of the resistivity data within a search radius from the EL, with defined regular depth intervals. Although it is shown here on a cross section, in practice, the search domain is a circular area centered on the EL. Figure 5 illustrates the variability of the estimation domain by plotting the AEM data locations for the 312 survey area and, for a single EL, every fifth search radius. Viewing the schematic in Figure 4, we can see that there is a link between the layer thicknesses, in the 1D resistivity models in the estimation domain (as defined by the search radius), and the expected minimum error in the TSZ estimate. A TSZ estimate is entirely based on assessing the resistivity distributions compiled from several 1D resistivity models within the estimation domain, so the TSZ estimate cannot be more accurate than the resolution, that is, the layer thickness, of these 1D resistivity models. The resolution of the 1D models in the estimation domain will be very similar in magnitude, so we defined the expected minimum error in each TSZ estimate to be the layer thickness, at the depth of the TSZ estimate, in the 1D resistivity model at the TSZ EL.

A key part of our methodology is the requirement that the above workflow is followed in each survey area where there is a need to identify the depth of the TSZ in the AEM data. That is, we recognize that there are two parameters — the search radius and the

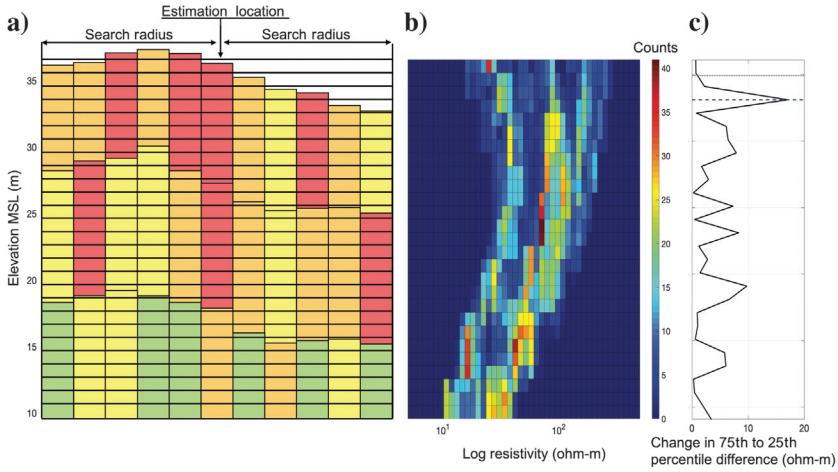

Figure 4. Schematic illustrating the process of estimating the TSZ at an EL from a 2D resistivity profile. (a) Each vertical column of cells represents a single 1D resistivity model with each colored cell representing a layer in the resistivity model; the variation in color is intended to show the variable resistivity. The horizontal black lines are the 1 m thick regular depth intervals, and the search radius is the distance within which the resistivity values are used to build the depth-registered resistivity distributions. (b) Example of depth-registered resistivity distributions for a selected EL. Shown here are actual distributions. (c) Change in the difference between the 75th and 25th percentiles with depth, for the same EL as (b). The blue dashed line is the depth picked for the TSZ, whereas the blue dotted line is the WTE measurement from the nearby well.

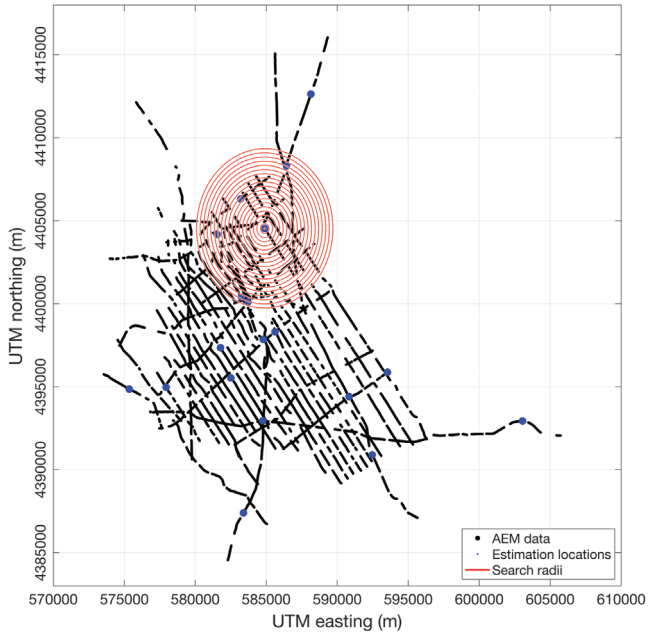

Figure 5. Plan-view map of the 312 survey area. AEM data are plotted in black. ELs are plotted as blue circles. For a selected EL, every fifth search radius is plotted in red.

statistical property of the resistivity distribution — that are likely to change depending on the survey area in terms of providing the best estimate of the TSZ, and we do not presume that the values for these parameters are transferrable from one area to another. Finding the optimal parameters for a specific survey area is a necessary step for obtaining the best possible estimates of the TSZ from the AEM data.

The final step in our methodology is to use the globally optimal combination of search radius and statistical property to produce a TSZ estimate at every AEM data acquisition location. We do this by selecting every 1D resistivity model produced from the AEM data in the given survey area, creating depth-registered resistivity distributions by gathering all of the resistivity values within the SR_{opt} and then identifying the depth at which there is the maximum change in the SP_{opt} as the TSZ. Due to the presence of geologic noise and the knowledge that the water table varies smoothly, a locally weighted linear regression filter that also removes outliers more than six standard deviations away from the mean is applied to the final TSZ estimates. This filter was applied using the smooth function in MATLAB with a smoothing radius of 0.2. This filtering may be unnecessary if there is limited noise present in a survey area, or it may be necessary to apply additional filters in areas with a higher level of noise. The final estimates provide the information that we are seeking: the depth to the TSZ, at the time of the acquisition of the AEM data, at all locations where we have AEM data.

In this study, two inversion methods (sharp and smooth) were used on the data from the 312 and 304 survey areas. We followed the above workflow for the analysis of the resistivity models derived using both inversion methods. This allowed us to investigate the impact of the inversion method on the SR_{opt} and SP_{opt} and on the accuracy of the final TSZ estimates.

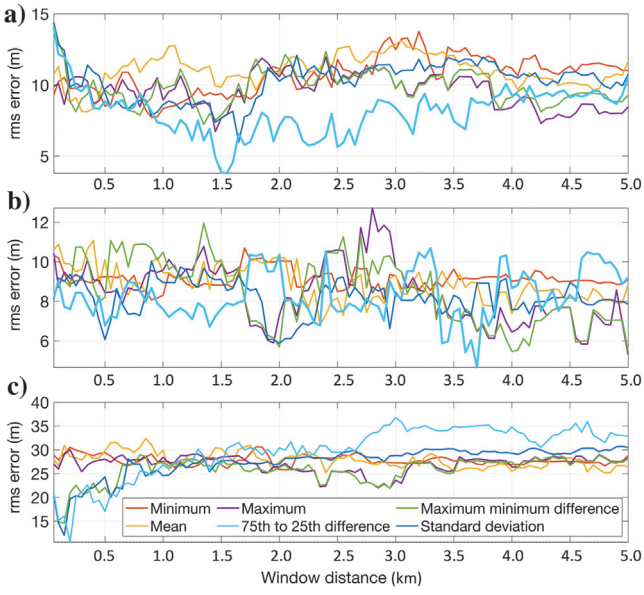

Figure 6. The rms error for each statistical property plotted as a function of the search radius. (a) Sharp inversion from the 312 survey area. (b) Sharp inversion from the 304 survey area. (c) Tulare survey area.

RESULTS

The rms error between each estimated TSZ and the corresponding WTE for every tested statistical property and search radius is shown in Figure 6. The smooth inversion results were similar to those presented in Figure 6 and are thus omitted. We expected the rms error to initially decrease with the increasing search radius because more 1D models contributed to the resistivity distribution and then begin to increase as the search radius became so large that the depth to the TSZ began to change more than the resolution of the ID models. Although we see this behavior in the results from the 312 and Tulare survey areas, it is less apparent in the results from the 304 area; this will be discussed in the next section.

Based on the results in Figure 6, the best TSZ estimates for all of the areas were made using the difference between the 75th and 25th percentiles as the statistical property. Other percentile differences (such as the difference between the 85th and 15th) also were initially tested, but the results were not significantly different from those obtained with the 75th and 25th. Also, we infer that the SR_{opt} for the 312 survey area was 1550 m, for the 304 survey area it was 3700 m, and for the Tulare area it was 200 m. These best estimates of the TSZ have an rms error of 3.8 m for the 312 area, 4.6 m for the 304 area, and 10.6 m for the Tulare survey area. The optimal combinations of statistical property and search radius and the associated rms errors for all of the inversions and survey areas used in this study are summarized in Table 1. We include, for comparison, the range of layer thicknesses in the 1D resistivity models at the estimated TSZ depths and locations. At each EL, we defined the expected minimum error in the TSZ estimate to be the layer thickness in the 1D resistivity model at the estimated depth of the TSZ.

Figure 7 shows three crossplots, each of which displays the best estimates of the TSZ versus the WTE measured in the testing and validation wells. The vertical error bars show the magnitude of the expected minimum error in the TSZ estimates; the deeper the TSZ,

Table 1. Optimal combination of the statistical property and the search radius, the associated rms error and, at the ELs, the range of layer thicknesses in the 1D resistivity models at the estimated TSZ depths, for each survey area and inversion.

Survey area	Inversion	SP_{opt}	SR_{opt} (m)	rms error (m)	Layer thickness (m)
312	Sharp	75th to 25th percentile	1550	3.8	3.0–3.7
312	Smooth	75th to 25th percentile	1550	5.3	3.0–3.9
304	Sharp	75th to 25th percentile	3700	4.6	1.3–2.8
304	Smooth	75th to 25th percentile	3700	4.8	1.1–2.5
Tulare	Semismooth	75th to 25th percentile	200	10.6	6.0–9.5

the thicker the layers in the 1D resistivity models so the more uncertain the TSZ estimates become. Across all ELs, the average layer thickness in the 1D resistivity models at the locations and depths of the TSZ estimates is 3.3 m for the 312 survey area, 1.9 m for the 304 survey area, and 8 m for the Tulare survey area.

Figures 8–11 show examples of the final results obtained by our methodology along flight lines from the sharp inversion of the AEM data acquired in the 312 and 304 survey areas. The geology shown in the cross section Figures 8–10 is a portion of the mixed coarse and fine packages that make up the upper aquifer. Figure 11 differs from Figures 8–10 in that it is a plot in plan view of the final filtered TSZ estimates at every AEM data location in the 312 and 304 survey areas. We note that it is not possible to identify the TSZ in a resistivity cross section based on observed changes in resistivity alone; we need to use changes in the distribution. We also see that in the far-right portion of the cross section in Figure 8, where the terrain starts to rise due to the foothills at the valley wall, the agreement between the TSZ estimates and the well measurement is worse than in the rest of the cross section. The TSZ estimate also appears to perform poorly in the far-right section of the cross section in Figure 10, but there is no nearby well measurement for validation.

DISCUSSION

The first step in our methodology was to define the SP_{opt} and search radius to be used in estimating the depth to the TSZ, with the results shown in Figure 6. Let us consider the results from the Tulare survey area, focusing first on the statistical properties. We see that the rms errors obtained using the statistical parameters, the minimum, the maximum, and the mean, show little variation with the search radius and never achieve the low errors obtained using the three statistical parameters that characterize the width of the resistivity distribution (the difference between the 75th and 25th percentiles, the difference between the maximum and minimum, and the standard deviation). What we observe is that the statistical properties that characterize the width of the distributions are the best estimators of the TSZ in the Tulare area. Based on the results in Figure 6, we identified the difference between the 75th and 25th percentiles as the optimal property, but we note that the other two properties characterizing distribution width produce similar rms errors.

The finding that there is a change in the width of the resistivity distribution at the TSZ is to be expected. Above the TSZ, saturated and unsaturated fine- and coarse-grained layers are possible. Fine-grained materials, such as clays, may retain water long after they are no longer surrounded by saturated materials. Coarse-grained materials (e.g., sands and gravels) could still be saturated above the TSZ due to water perched on top of less permeable clays. Below the TSZ, the fine- and coarse-grained layers will be fully saturated, resulting in a narrower distribution of resistivity values below than above the TSZ. It is possible that a laterally consistent change in lithology at some depth could result in a narrowing of the resistivity distribution similar to what would be caused by the TSZ. If this were to occur within the anticipated depth interval of the TSZ, it could lead to the false identification of that depth as corresponding to the TSZ. In this case, knowledge of the local geology would be needed to assess the probability of this occurrence. In our

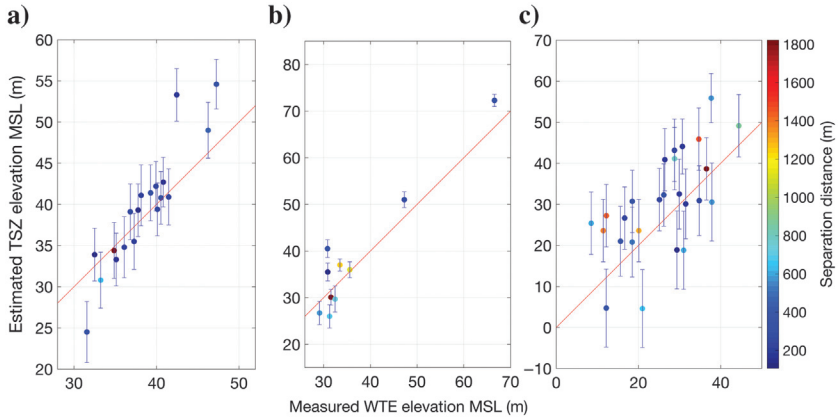

Figure 7. All plots show the estimated TSZ elevation versus the measured WTE. (a) Results for the sharp inversion of the AEM data from the 312 survey area using the difference between the 75th and 25th percentiles with a search radius of 1550 m. (b) Results for the sharp inversion of the AEM data from the 304 survey area using the difference between the 75th and 25th percentiles with a search radius of 3700 m. (c) Results for the Tulare survey area using the difference between the 75th and 25th percentiles with a search radius of 200 m. The red line on the plots indicates the one-to-one line. The color of the plotted circles represents the separation distance between the EL and the corresponding WTE measurement. The error bars are the layer thickness in the 1D resistivity model at the location and depth of the TSZ estimate, defined as the expected minimum error in the TSZ.

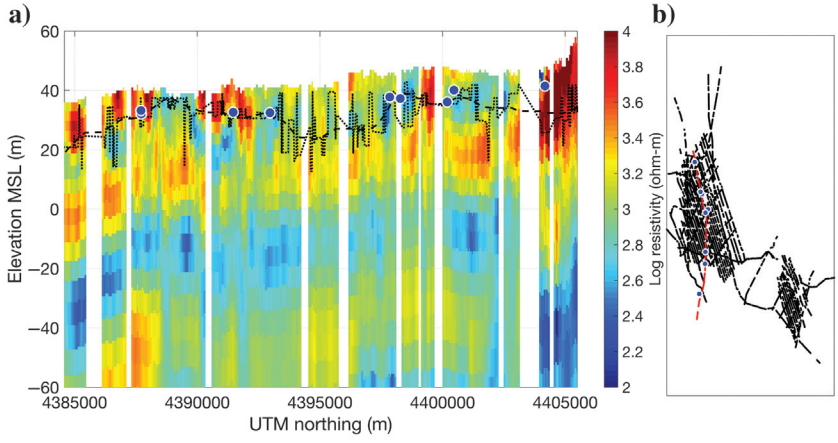

Figure 8. (a) Resistivity cross section of line 710201 from the sharp inversion of the AEM data from the 312 survey area. The dashed black line indicates the estimated depth to the TSZ. The dotted black line indicates the estimated depth to the TSZ before application of the locally weighted linear regression filter. The blue circles with white outlines are the locations of wells with WTE measurements within 2 km of the selected flight line. (b) The location of the selected line in relation to the 312 and 304 survey areas.

DOI:10.1190/geo2019-0539.1

survey areas, it was clear from descriptions of the local geology (Faunt, 2009; McManus et al., 2014) that this type of false identification was not a problem.

Let us now consider the selection of the SR_{opt}, again referring to the results for the Tulare area. For the statistical properties characterizing the distribution width, the rms error shows the dependence on search radius that we expected to see: first a decrease in rms error, presumably due to the increase in the number of 1D resistivity models used in the TSZ estimation, and then an increase in rms error likely due to the expansion of the search radius to the point at which the depth to the TSZ starts to vary from the depth at the EL. The form of the dependence in the Tulare area led us to easily identify 200 m as the SR_{opt}.

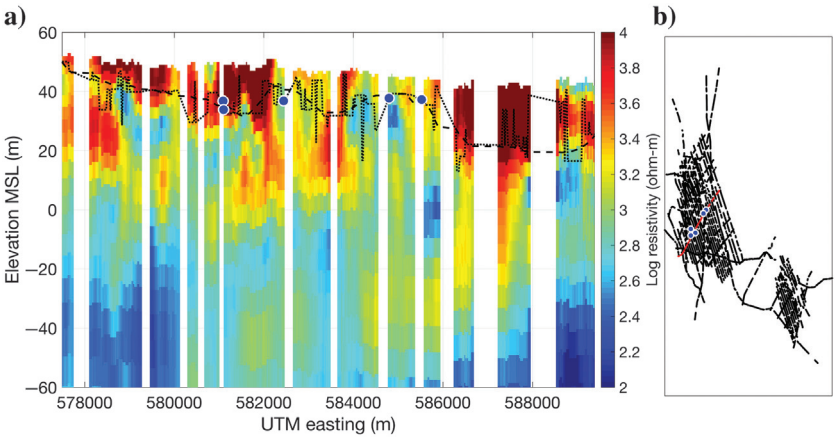

Figure 9. (a) Resistivity cross section of line 200601 from the sharp inversion of the AEM data from the 312 survey area. The dashed black line indicates the estimated depth to the TSZ. The dotted black line indicates the estimated depth to the TSZ before application of the locally weighted linear regression filter. The blue circles with the white outlines are the locations of wells with WTE measurements within 2 km of the selected flight line. (b) The location of the selected line in relation to the 312 and 304 survey areas.

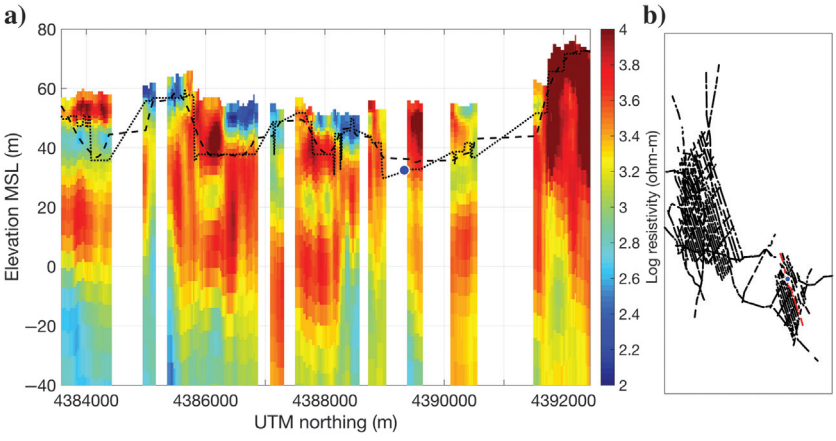

Figure 10. (a) Resistivity cross section of line 300801 from the sharp inversion of the AEM data from the 304 survey area. The dashed black line indicates the estimated depth to the TSZ. The dotted black line indicates the estimated depth to the TSZ before application of the locally weighted linear regression filter. The blue circles with the white outlines are the locations of wells with WTE measurements within 1 km of the selected flight line. (b) The location of the selected line in relation to the 312 and 304 survey areas.

The results for the 312 area are similar in form to those for the Tulare area but with less difference in the rms errors (note the change in scale in the vertical axes in Figure 6). The difference between the 75th and 25th percentiles emerged as the SP_{opt}, with a clearly defined rms minimum at a search radius of 1550 m.

The results for the 304 area show a much more complex dependence of the rms error on the statistical property and search radius. Although the difference between the 75th and 25th percentiles produces the lowest rms errors for most of the search radii, there is not a simple error dependence on the search radius. We selected the difference between the 75th and 25th percentiles as the SP_{opt} and 3700 m as the SR_{opt}, but we acknowledge less confidence in the results than in the other two survey areas. We return to these observations below when we discuss the errors in TSZ estimates found in the three survey areas.

Let us now assess the accuracy of our TSZ estimates, starting first with the Tulare survey area. In this survey area, there were no continuously monitored wells and the WTE measurements were collected two to four weeks before the acquisition of the AEM data. The best estimates of the TSZ in the Tulare area had an rms error of 10.6 m. This is a surprisingly good result because it is only approximately 30% larger than the 8 m average of the layer thicknesses at the locations and depths of the TSZ estimates, defined as the expected minimum error. In Figure 7, the color of the plotted points indicates the separation distance between the TSZ ELs and the WTE measurements; we expected this to impact the results from the Tulare area where the survey was not designed to acquire data close to the wells where WTE measurements are made. However, we found no correlation between the separation distance and the rms error.

The crossplot in Figure 7c illustrates the presence of bias in the relationship between the TSZ estimates and the WTE measurements, with a majority of the TSZ estimates lying above the one-to-one line; this indicates that the TSZ is being positioned at higher elevations, or shallower depths, than the WTE measured in the wells. During the summer months, there is extensive groundwater pumping in Tulare County that tapers off after the first harvests in August and September. We would expect to see the WTE, depressed by the summer pumping, start to rebound in September and October once pumping is reduced. Our interpretation is that the rebound in WTE, between the time of the well-based WTE measurements in mid-September to early October, and the acquisition of the AEM data in mid-October, is the main source of error and the cause of the bias present in the TSZ estimates.

The results from the 312 survey area illustrate the accuracy possible from our methodology when the temporal and spatial separation between the AEM data and the WTE measurements

DOI:10.1190/geo2019-0539.1

are minimized by (1) acquiring WTE measurements from wells during AEM data acquisition and (2) locating flight lines close to the wells. Our methodology produced TSZ estimates with rms errors of 3.8 and 5.6 m for the sharp and smooth inversions, respectively, with no apparent bias observed in Figure 7. These values for the errors are 15% and 70% higher than the expected minimum error for the sharp and smooth inversions, respectively, as defined using the layer thicknesses in the 1D resistivity models. In this survey area, we had the two forms of inversion, allowing us to assess the impact of the inversion on the results. We attribute the lower error obtained using a sharp inversion to the inversion method producing resistivity models that retain large vertical changes in resistivity that are smoothed out in the smooth inversion. Given that the top of the TSZ should correspond to a relatively large change in resistivity, smoothing out this resistivity change will reduce the impact of the TSZ on the depth-registered resistivity distributions, making the TSZ more difficult to accurately locate.

In the 304 survey area, our methodology produced TSZ estimates with rms errors of 4.6 m for the sharp inversion and 4.8 m for the smooth inversion; these correspond to 120% and 160% larger than the expected minimum error, as defined using the layer thicknesses in the 1D resistivity models for the sharp and smooth inversions, respectively. The level of error present and the form of the relationship between the rms error and the search radius seen in Figure 6 makes it clear that our developed methodology does not perform as well in the 304 survey area as it does in the other two areas.

We identify two likely causes for the decreased performance of our methodology in the 304 survey area, the first of which affects our ability to define a SR_{opt} that is valid for the entire survey area. The SR_{opt} is defined by an observed minimum in the rms error of the TSZ estimates. The rms error will decrease with increasing search radius as we add more 1D resistivity models to the estimation domain until we expand to the point where we encounter significantly different TSZ values, at which point it starts to increase; thus, the SR_{opt} represents a trade-off in the estimation domain between the number of 1D resistivity models and the variability of the TSZ. If the spatial density of 1D resistivity models varies within the survey area, it becomes challenging to define a single SR_{opt}.

The number of 1D resistivity models in an estimation domain varies considerably over the 304 survey area due to the removal of data impacted by EM noise from the infrastructure. This was not a uniform removal of data, but it resulted in variability in the spatial density of 1D resistivity models making it challenging to define one SR_{opt} for the entire survey area. Variable flight line spacing over a survey area also could have a similar effect on the results of our methodology. Because all of our survey areas had regularly spaced flight lines, this was not an issue. This uneven removal of data explains the behavior seen in Figure 6 for the 304 survey area. Applying one search radius in estimating TSZ for the entire area, as we have done, will result in increased error at any given EL where that is not the optimal radius.

The second likely cause is terrain roughness. Our estimates of the TSZ are based on 1D resistivity models assumed to start at the ground surface. The determination of the ground surface elevation uses measurements from two laser altimeters mounted on the AEM system. These altimeters will be pitched up or down in rough terrain, resulting in measurement errors that affect the accuracy of the TSZ estimates. Approximately half of the 304 survey area was in the foothills at the valley edge resulting in greater terrain roughness than in the other two survey areas.

The rms errors found in all three survey areas are large when compared to the accuracy of well-based measurements of WTE, which have reported accuracies on the scale of centimeters (Laird et al., 2016). However, our motivation for developing this methodology for determination of the TSZ is not to replace well-based WTE measurements; rather, it is to estimate the TSZ in a geologically heterogeneous area at every location where AEM data were acquired at the time of acquisition. These TSZ estimates will be used to divide the resistivity model into the unsaturated and saturated domains, allowing for the development and application of two separate resistivity-lithology transforms for the two saturation states. Given that the largest rms errors in the TSZ estimates are only approximately 2.5 times larger than the average layer thickness in the resistivity models at the depth of the TSZ estimates, the TSZ will be placed within a layer or two of the correct layer in the resistivity models when developing and applying the resistivity-lithology transforms.

When examining the results in plan view (shown in Figure 11), we see spatial variation in the TSZ over much shorter distances than in the previously available interpolated WTE contours plotted in Figure 1. We see several small regions in Figure 11 with a TSZ that is deeper than in the areas surrounding it. Because the 312 and 304 survey areas are agricultural areas with active pumping, these zones of lowered TSZ are presumably cones of depression due to pumping. The largest cone of depression is near the center of the figure and is indicated with the red letter A. Referring to Figure 1, we also see this cone of depression in the plotted WTE contours and note that it is most likely caused by domestic pumping in the city of Chico. The other smaller cones of depression are not captured in Figure 1, likely due to the low spatial density of the measurements upon which the WTE contours are based. We also note that the AEM data were acquired in the first few days of December, whereas the contours plotted in Figure 1 are from CASGEM measurements in September and October. Thus, even given a sufficient spatial density of WTE measurements, we would not expect the TSZ estimates

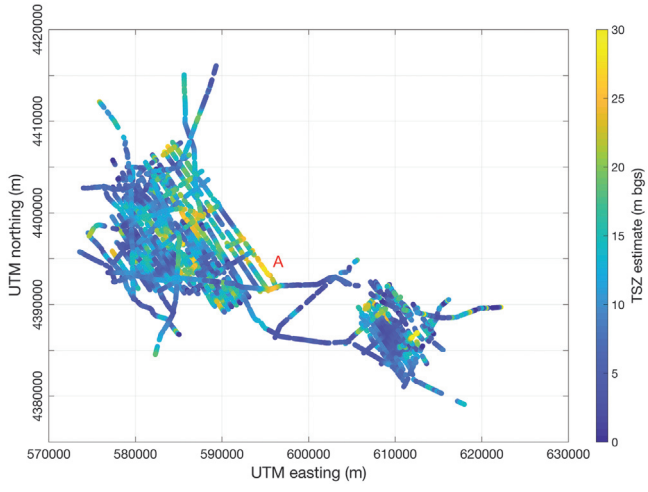

Figure 11. Plan-view map of the final filtered TSZ estimates for the 312 and 304 survey areas. The color of the points represents the depth below the ground surface of the estimated TSZ. The letter A in the middle of the figure indicates an area with localized drawdown of the TSZ.

DOI:10.1190/geo2019-0539.1

from December, after significant pumping for irrigation has taken place, to match the WTE contours from September/October. Ultimately, the spatial variation seen in the TSZ estimates in Figure 11 reinforces the necessity for our developed methodology. Without it, the small cones of depression in the figure would be missed and would likely result in incorrect interpretation of the resistivity models in those areas.

We assume that others applying this methodology in new areas will use all of the WTE measurements available. An obvious issue to address is the impact of the number of WTE measurements on the ability to determine the SP_{opt} and SR_{opt} and thus accurately estimate the TSZ. We addressed this by conducting a bootstrap analysis (Johnson, 2001) for all three survey areas by randomly selecting, with replacement, subsets of 1 to 10 WTE measurements from the full set of WTE measurements in each survey area. In total, 10,000 iterations of this random selection were performed for each subset size. We then went through the full workflow, determining the SR_{opt} and SP_{opt} for each iteration and subset of WTE measurements, for each survey area and resistivity model. We found that using three or more WTE measurements yielded, for each survey area, for a majority of the iterations, the same optimal combination (i.e., a search radius of 1550 m and the difference between the 75th and 25th percentiles for the sharp inversion AEM data from the 312 survey area) that was found using all of the WTE measurements. That is, on average, only three randomly selected WTE measurements were required to find the optimal parameters for estimating the TSZ in each survey area. Thus, while a large number of wells were used in each survey area to develop the methodology presented within this study, future applications of this method should only require approximately three wells per approximately 600 km^2 of survey area covered (i.e., the approximate size of the 312 survey area).

CONCLUSION

In this study, we developed and tested a new methodology to map the TSZ from AEM data with sufficient accuracy to inform the development and application of resistivity-lithology transforms that account for the saturation state. The spatial information about the TSZ retrieved by this methodology will greatly reduce the uncertainty present when interpreting changes in a resistivity model produced from an AEM data set that includes data from saturated and unsaturated zones. Reviews of previous literature revealed that the impact of the TSZ on AEM data generally has been ignored. When it was accounted for, this was done using well-based measurements of the WTE that did not fully capture the true spatial and temporal variation in the TSZ at the time of the AEM survey. The benefits of using the developed methodology can be realized in any area where AEM data are acquired from saturated and unsaturated zones; however, these benefits will be greatest in areas with significant spatial or temporal fluctuations in the TSZ, or with few well-based measurements of WTE. Although we have developed and applied the methodology using time-domain AEM data, it can be applied to data collected with frequency-domain AEM systems.

For the specific AEM data sets used here, we conclude that the optimal search radii were large enough to include a sufficient number of 1D resistivity models, although they were not so large that the TSZ changed significantly. These optimal search radii were found to be independent of the vertical constraints applied during the inversion. However, the vertical constraints did impact the resulting accuracy of the TSZ estimates with sharp inversions producing more accurate estimates. We found that in the 304 survey area, the uneven removal of data due to infrastructure noise resulted in the presence of multiple optimal search radii and thus reduced the performance of our methodology when compared to that obtained in the other survey areas. This suggests that the key information influencing the SR_{opt} is some measure of the spatial variability in the TSZ relative to the spatial density of the AEM data.

There are some conclusions that can be drawn from this study about the search radius that can inform the transfer of this methodology to other locations: (1) The maximum search radius tested should be informed by the regional groundwater gradient, and (2) the step size at which the search radius is increased should be large enough to ensure that, given the spatial distribution of AEM soundings, the number of soundings used increases with each increase in the search radius.

We found that for all of the combinations of survey area and inversion type, the SP_{opt} was the difference between the 75th and 25th percentiles; other properties that characterize the width of the distribution yielded similar but worse results. We conclude that these properties always will be the ones most sensitive to the saturation state, so in an area with limited access to WTE measurements, we would recommend the use of a set of properties that contain information about the width of the resistivity distribution.

Here, we have assumed that measurements of WTE provide a good estimate of the TSZ, but this would need to be assessed in any area where this methodology is to be applied. If it was determined that a more accurate measure of the TSZ was needed or if the capillary fringe was found to be an issue, geophysical logging measurements could be used to complement WTE measurements in wells and locate the TSZ.

The developed methodology, when optimized for local conditions, can be used to produce the best possible estimates of the TSZ from the AEM data acquired in a survey area. Due to the TSZ's impact on the relationship between resistivity and lithology, the ability to estimate the TSZ from the AEM data can dramatically improve the accuracy of a resistivity-lithology transform and it thus represents a significant contribution to advancing the adoption of airborne geophysics for mapping and managing groundwater systems. A goal for future development of this methodology is to identify guidelines for the optimal search radius and statistical property for various geologic environments and hydrologic conditions, allowing for the estimation of the TSZ from AEM data in areas with few or no WTE measurements.

ACKNOWLEDGMENTS

Funding for this research was provided by the Ministry of Environment and Food of Denmark, the Ecoinnovation Programme (grant no. MST-117-00388) and the California Department of Water Resources (grant no. 4600012515) through the Stanford Groundwater Architecture Project (mapwater.stanford.edu), and from the Gordon and Betty Moore Foundation (grant no. GBMF6189). We would like to thank our local partners in the Butte County Department of Water and Resource Conservation (BCDWRC), the Glenn County Department of Water Resources, and the California Department of Water Resources for assistance with obtaining the water level data, C. Buck from BCDWRC and T. Greene at Chico State for their assistance during the planning of the airborne electro-

magnetic survey, and Aqua Geo Frameworks for providing the processed airborne electromagnetic data. We also would like to thank I. Gottschalk and S. Kang for numerous helpful discussions and several anonymous reviewers for their comments and suggestions.

DATA AND MATERIALS AVAILABILITY

Data associated with this research are confidential and cannot be released.

APPENDIX A

AEM SYSTEMS

Table A-1 contains additional technical details for the three SkyTEM systems that acquired the AEM data used in this paper.

REFERENCES

Asch, T., J. Abraham, and J. Cannia, 2019, Hydrogeologic framework of selected areas in Butte and Glenn Counties, California, Mitchell, Nebraska, Aqua Geo Frameworks, http://www.buttecounty.net/wrcdocs/Reports/SpecialProjects/AEM/AGF-AEM_Report_2019.pdf.

Auken, E., A. V. Christiansen, J. H. Westergaard, C. Kirkegaard, N. Foged, and A. Viezzoli, 2009, An integrated processing scheme for high-resolution airborne electromagnetic surveys, the SkyTEM system: Exploration Geophysics, **40**, 184–192, doi: 10.1071/EG08128.

Auken, E., A. V. Christiansen, C. Kirkegaard, G. Fiandaca, C. Schamper, A. A. Behroozmand, A. Binley, E. Nielsen, F. Effersø, N. B. Christensen, K. Sørensen, N. Foged, and G. Vignoli, 2015, An overview of a highly versatile forward and stable inverse algorithm for airborne, ground-based and borehole electromagnetic and electric data: Exploration Geophysics, **46**, 223–235, doi: 10.1071/EG13097.

Behroozmand, A. A., E. Auken, and R. Knight, 2019, Assessment of recharge sites using a new geophysical imaging method: Vadose Zone Journal, **18**, 1–13, doi: 10.2136/vzj2018.10.0184.

Binley, A., S. S. Hubbard, J. A. Huisman, A. Revil, D. A. Robinson, K. Singha, and L. D. Slater, 2015, The emergence of hydrogeophysics for improved understanding of subsurface processes over multiple scales: Water Resources Research, **51**, 3837–3866, doi: 10.1002/2015WR017016.

Table A-1. System specifications for SkyTEM 304, 312, and 508.

SkyTEM 304		
Parameter	Low moment	High moment
No. of transmitter turns	1	4
Transmitter area per turn	342 m^2	342 m^2
Transmitter current	~9 Amp	100–120 Amp
Transmitter dipole	Vertical	Vertical
Peak moment	2700 NIA	Up to 150,000 NIA
On time	800 μs	10 ms
Off time	1581 μs	12.222 ms
Rep. frequency	210 Hz	22.5 Hz
Power supply	External DC generator, part of the sling load	
SkyTEM 312		
No. of transmitter turns	2	12
Transmitter area per turn	340 m^2	340 m^2
Transmitter current	~9 Amp	100–120 Amp
Transmitter dipole	Vertical	Vertical
Peak moment	3000 NIA	Up to 500,000 NIA
On time	800 μs	4 ms
Off time	1581 μs	12.666 ms
Rep. frequency	210 Hz	30 Hz
Power supply	External DC generator, part of the sling load	
SkyTEM 508		
No. of transmitter turns	1	8
Transmitter area per turn	536 m^2	536 m^2
Transmitter current	~7 Amp	100–120 Amp
Transmitter dipole	Vertical	Vertical
Peak moment	4000 NIA	500,000 NIA
On time	800 μs	5 ms
Off time	1018 μs	15 ms
Rep. frequency	275 Hz	25 Hz
Power supply	External DC generator, part of sling load	

Bryan, K., 1923, Geology and ground-water resources of Sacramento Valley, California, https://www.waterboards.ca.gov/waterrights/water_issues/programs/bay_delta/docs/cmnt081712/sldmwa/bryangroundwaterforirrigationinthesacramentovalley.pdf, accessed 6 August 2019.

California Department of Water Resources, 2020a, Groundwater information center interactive map application, https://gis.water.ca.gov/app/gicima/, accessed 8 August 2019.

California Department of Water Resources, 2020b, Water data library, http://wdl.water.ca.gov/waterdatalibrary/docs/Hydstra/, accessed 8 August 2019.

Chongo, M., A. V. Christiansen, G. Fiandaca, I. A. Nyambe, F. Larsen, and P. Bauer-Gottwein, 2015, Mapping localised freshwater anomalies in the brackish paleo-lake sediments of the Machile–Zambezi basin with transient electromagnetic sounding, geoelectrical imaging and induced polarisation: Journal of Applied Geophysics, **123**, 81–92, doi: 10.1016/j.jappgeo.2015.10.002.

Christiansen, A. V., N. Foged, and E. Auken, 2014, A concept for calculating accumulated clay thickness from borehole lithological logs and resistivity models for nitrate vulnerability assessment: Journal of Applied Geophysics, **108**, 69–77, doi: 10.1016/j.jappgeo.2014.06.010.

Cook, P. G., and S. Kilty, 1992, A helicopter-borne electromagnetic survey to delineate groundwater recharge rates: Water Resources Research, **28**, 2953–2961, doi: 10.1029/92WR01560.

Faunt, C. C., ed., 2009, Groundwater availability of the Central Valley aquifer, California: United States Geologic Survey.

Fetter, C. W., 2000, Applied hydrogeology: Pearson.

Fitterman, D. V., and M. Deszcz-Pan, 2001, Using airborne and ground electromagnetic data to map hydrologic features in Everglades National Park: Proceedings of the 14th EEGS Symposium on the Application of Geophysics to Engineering and Environmental Problems.

Foged, N., P. A. Marker, A. V. Christansen, P. Bauer-Gottwein, F. Jørgensen, A. S. Høyer, and E. Auken, 2014, Large-scale 3-D modeling by integration of resistivity models and borehole data through inversion: Hydrology and Earth System Sciences, **18**, 4349–4362, doi: 10.5194/hess-18-4349-2014.

Foley, N., S. Tulaczyk, E. Auken, C. Schamper, H. Dugan, J. Mikucki, R. Virginia, and P. Doran, 2016, Helicopter-borne transient electromagnetics in high-latitude environments: An application in the McMurdo Dry Valleys, Antarctica: Geophysics, **81**, no. 1, WA87–WA99, doi: 10.1190/geo2015-0186.1.

Greene, T. J., and K. Hoover, 2014, Hydrostratigraphy and pump-test analysis of the lower Tuscan/Tehama aquifer, Northern Sacramento Valley, CA, Chico, California, Chico State Department of Geologic and Environmental Sciences, Final Report, https://www.csuchico.edu/cwe/_assets/documents/final-report-lower-tuscan-project-compressed.pdf.

Høyer, A. S., F. Jørgensen, P. B. E. Sandersen, A. Viezzoli, and I. Møller, 2015, 3D geological modelling of a complex buried-valley network delineated from borehole and AEM data: Journal of Applied Geophysics, **122**, 94–102, doi: 10.1016/j.jappgeo.2015.09.004.

HydroGeophysics Group, 2011, Guide for processing and inversion of SkyTEM data in the Aarhus Workbench, Aarhus, Denmark, Aarhus University Department of Earth Sciences, Version 2.0, http://www.hgg.geo.au.dk/rapporter/guide_skytem_proc_inv.pdf.

Johnson, R. W., 2001, An introduction to the Bootstrap: Teaching statistics, **23**, 49–54, doi: 10.1111/1467-9639.00050.

Knight, R., R. Smith, T. Asch, J. Abraham, J. Cannia, A. Viezzoli, and G. Fogg, 2018, Mapping aquifer systems with airborne electromagnetics in the Central Valley of California: Groundwater, **56**, 893–908, doi: 10.1111/gwat.12656.

Laird, J., M. Cowin, G. Bardini, T. Ravazzini, J. Pacheco, W. Croyle, and K. Kishaba, 2016, Status report on implementation of the California statewide groundwater elevation monitoring program years 2012–2015, Sacramento, California, Department of Water Resources, https://cawaterlibrary.net/document/submittal-of-report-status-report-on-implementation-of-the-california-statewide-groundwater-elevation-monitoring-program-years-2012-2015/.

Luhdorff and Scalmanini Consulting Engineers, 2016, Central Valley salinity alternatives for long term sustainability (CV-SALTS), region 5: Updated groundwater quality analysis and high resolution mapping for Central Valley salt and nitrate management plan, San Joaquin Valley, California, https://www.cvsalinity.org/docs/committee-document/technical-advisory-docs/conceptual-model-development/3306-updated-groundwater-quality-analysis-and-high-resolution-mapping-for-central-valley-salt-and-nitrate-management-plan/file.html.

Madsen, L. M., K.V. Lassen, E. Auken, and A.V. Christiansen, 2017, Comparison of near-surface sensitivity functions of airborne and ground-based EM systems: Proceedings of the Second European Airborne Electromagnetics Conference.

McManus, D., K. Staton, and D. Spangler, 2014, Geology of the Northern Sacramento Valley, California, Sacramento, California, Department of water resources, https://cawaterlibrary.net/document/geology-of-the-northern-sacramento-valley-california/.

Paine, J. G., 2003, Determining salinization extent, identifying salinity sources, and estimating chloride mass using surface, borehole, and airborne electromagnetic induction methods: Water Resources Research, **39**, HWC1–HWC10, doi: 10.1029/2001WR000710.

Peterson, K., 2018, 2018 water quality memo, Butte, California, Butte County Department of water and resource conservation, http://www.buttecounty.net/wrcdocs/Programs/Monitoring/GWQuality/2018WaterQuality_memo.pdf.

Podgorski, J. E., A. G. Green, T. Kalscheuer, W. K. H. Kinzelbach, H. Horstmeyer, H. Maurer, L. Rabenstein, J. Doetsch, E. Auken, T. Ngwisanyi, G. Tshoso, B. C. Jaba, O. Ntibinyane, and K. Laletsang, 2015, Integrated interpretation of helicopter and ground-based geophysical data recorded within the Okavango Delta, Botswana: Journal of Applied Geophysics, **114**, 52–67, doi: 10.1016/j.jappgeo.2014.12.017.

Sørensen, K. I., and E. Auken, 2004, SkyTEM — A new high-resolution transient electromagnetic system: Exploration Geophysics, **35**, 191–199, doi: 10.1071/EG04194.

Spies, B. R., 1989, Depth of investigation in electromagnetic sounding methods: Geophysics, **54**, 872–888, doi: 10.1190/1.1442716.

Vignoli, G., G. Fiandaca, A. V. Christiansen, C. Kirkegaard, and E. Auken, 2015, Sharp spatially constrained inversion with applications to transient electromagnetic data: Geophysical Prospecting, **63**, 243–255, doi: 10.1111/1365-2478.12185.